Supporting Information

Bisalt Ether Electrolytes: A Pathway Towards Lithium Metal Batteries with Ni-rich Cathodes

Judith Alvarado[1,2†], Marshall A. Schroeder[1†], Travis P. Pollard[1,†], Xuefeng Wang[3], Jungwoo Z. Lee[3], Minghao Zhang [3], Thomas Wynn[2] Michael Ding[1], Oleg Borodin[1*], Ying Shirley Meng[2,3*], Kang Xu[1*]

1. Electrochemistry Branch, Sensors and Electron Devices Directorate, U.S. Army Research Laboratory, Adelphi, MD 20783, USA
2. Materials Science and Engineering, University of California San Diego, La Jolla, CA 92093, USA
3. Department of NanoEngineering, University of California San Diego, La Jolla, CA 92093, USA

[†]Equal contribution, [*]Corresponding Authors

Table S1. Electrolyte Concentration Conversions. Molarity values adapted from Qian et al.[2]

Mole Ratio (DME/Li)	Molality, m (mol salt/kg solvent)	Molarity[2] (mol salt/L solution)
1	**10.965**	**5M**
1.4	**7.8321429**	**4M**
1.6	**6.853125 (~6.9m)**	
2	**5.4825**	**3.6M**
2.2	**4.9840909**	**3M**
2.4	**4.56875 (~4.6m)**	
4	**2.74125**	**2M**
4.8	**2.284375 (~2.3m)**	
8.9	**1.2320225**	**1M**

Additional Details on Molecular Dynamics Simulation Methodology

The MD simulation package, WMI-MD (including many-body polarization) was used for all of the MD simulations. A copy of the simulation package, description of the input files was published as Supported Information for Borodin et al.[3] Force field parameters are provided in a separate file ff.dat-DME1.6-LiTFSI-LiFSI. The simulation box for bulk simulations contained 308 DME, 96 LiTFSI and 96 LiFSI. Initial dimensions were gradually decreased from 90 to 50 Å during a 3.2 ns initial simulation run at 500 K. NPT equilibration runs were then performed for 30 ns at 393 K, followed by 38 ns NVT runs at the density corresponding to 1 atm. After that temperature was dropped to 333 K, followed by 22.1 ns NPT runs and 68.8 ns NVT runs. A final configuration from 333 K run was used as a starting configuration for 298 K simulations that were performed for 48.5 ns in NPT ensemble followed by 39.3 ns run in NVT ensemble. NPT runs were treated as equilibration runs, while NVT runs were used for analysis and extracting structural and transport properties.

The Ewald summation method was used for the electrostatic interactions between permanent charges with either permanent charges or induced dipole moments with $k = 7^3$ vectors. Multiple timestep integration was employed with an inner timestep of 0.5 fs (bonded interactions), a central time step of 1.5 fs for all non-bonded interactions within a truncation distance of 7.0-8.0 Å and an outer timestep of 3.0 fs for all non-bonded interactions between 7.0 Å and the nonbonded

truncation distance of 16 Å. The reciprocal part of Ewald was calculated every 3.0 fs. A Nose-Hoover thermostat and a barostat were used to control the temperature and pressure with the associated frequencies of 10^{-2} and 0.1 x 10^{-4} fs. The stress tensor was saved every 3 or 9 fs for calculating the stress, the tensor autocorrelation function and the viscosity, while the atomic coordinates were saved every 2 ps for post-analysis.

The many-body polarizable APPLE&P force field was extended to DME in this work, while previously developed parameters for LiFSI and LiTFSI were used.[1, 4] DME charges were fit to electrostatic grid calculated at the MP2/aug-cc-pvTz, while torsional parameters were refit to conformational energies by calculated at MP2/aug-cc-pvTz at M05-2X/aug-cc-pvTz geometries. A detailed description of the APPLE&P is given elsewhere.[5]

Self-diffusion coefficients were extracted using Einstein relation and corrected for the finite size effects closely following previous work.[3, 6] The resulting self-diffusion coefficients are given in Table S2.

Table S2. Self-diffusion coefficients (in 10^{-10} m^2/s) of solvent (DME) and ions predicted by MD simulations of DME doped with 3.46 m LiFSI and 3.46m LiTFSI.

	393 K	333 K	298 K
DME	4.20	0.70	0.14
FSI^-	3.59	0.65	0.14
$TFSI^-$	2.81	0.59	0.12
Li^+	3.27	0.67	0.14

Table S3. Average coulombic efficiencies for lithium plating and stripping at various cycles.

Average Coulombic Efficiencies (Li vs. Cu)			
Cycles Sampled	**Gen II**	**SSEE**	**BSEE**
1st Cycle	54.74	82.72	82.11
First 20 Cycles	78.09	96.80	95.33
Next 180 Cycles	70.21	98.36	98.19
All 200 cycles	71.00	98.21	97.90

Lithium Anode Characterization

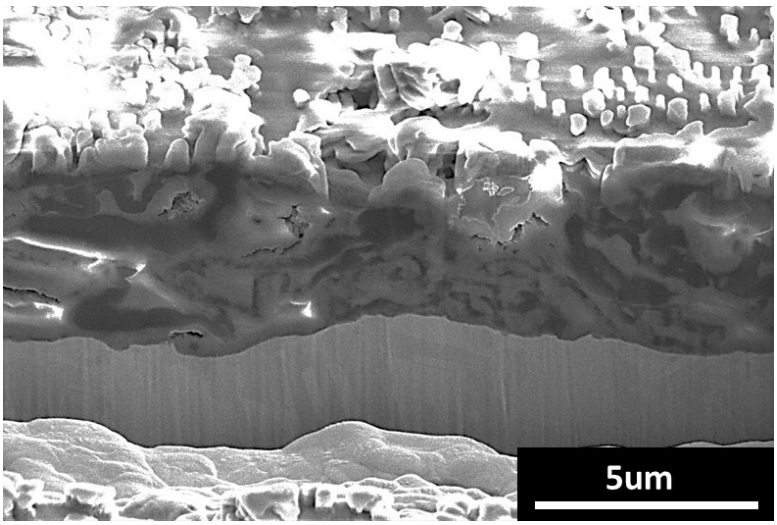

Figure S1. Cryo-FIB cross sectional image of deposited Li using 6.9m LiFSI-DME electrolyte using same protocol as Figure 3. Notice that significantly increasing LiFSI concentration does not result in improved plating morphology. The Li surface film also charged significantly under e-beam exposure.

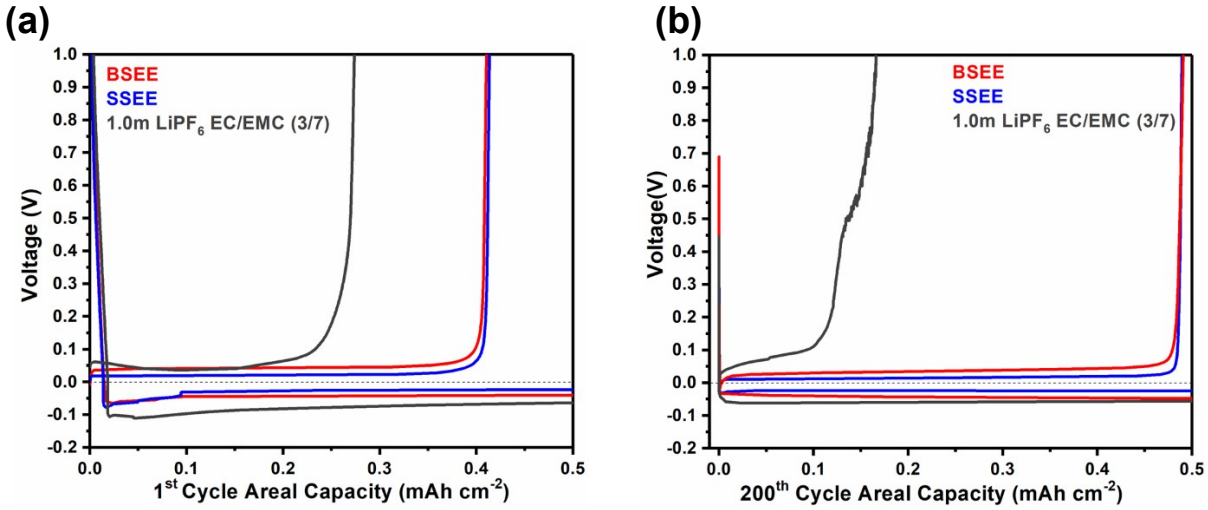

Figure S2. (a) Voltage profile of 1st and 100th (b) cycles of lithium versus copper cells with different electrolytes cycled at a rate of 0.5mA/cm² to a capacity of 0.5mAh/cm². Slightly higher overpotential for BSEE vs. SSEE is attributed to increased viscosity.

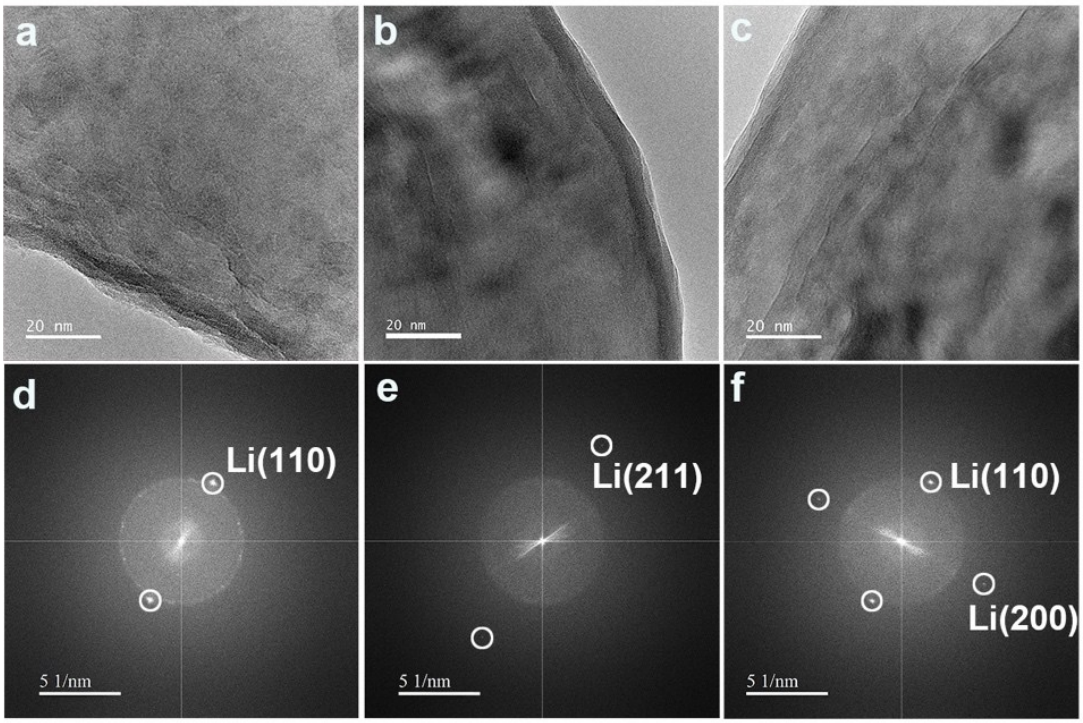

Figure S3. Cryo-TEM images of deposited Li using 4.6m LiFSI-DME (SSEE) electrolyte after 20 minutes of deposition at 0.5 mA cm^2.

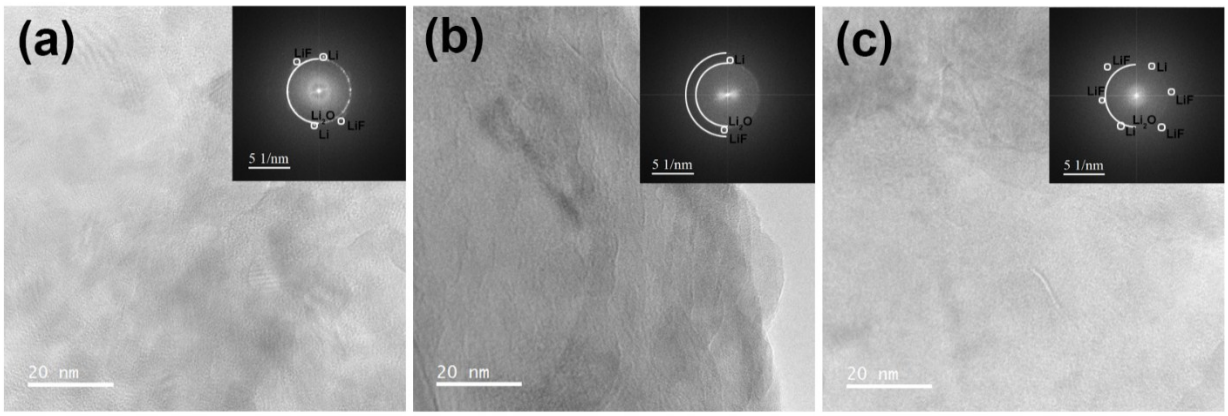

Figure S4. Cryo-TEM images of deposited Li using a) Gen II: 1.0m $LiPF_6$ EC/EMC b) SSEE and c) BSEE electrolyte after 20 minutes of deposition at 0.5 mA cm^{-2}. Some electron diffraction patterns of the ~50 images taken for each electrolyte showed trace signatures of crystalline LiF, albeit as a minority component of the SEI under these conditions.

Cryo-TEM: After the 20 minutes of deposition, the Li metal morphology is dominated by sheets with ribbons incorporated as well. Both the sheets and the ribbons are a combination of crystalline and amorphous Li metal, where the sheets are more likely to be amorphous compared to the dendrites. In addition the Li metal crystallizes from the joints to different orientations that is dominated by (110) but also contain (200) and (211) planes.

XPS:

Figure S5a shows the C1s spectra for all electrolytes, where the SEI generated by Gen II electrolyte is dominated by solvent (EC:EMC) decomposition products, forming ethers (CO, 286.6 eV), esters (OCO, 288.6 eV), and carbonate (CO_3, 289.9eV) moieties. The SEI generated by 4.6m LiFSI-DME also has similar functionalities that are associated with the decomposition of the DME solvent. The addition of LiTFSI demonstrates that the salt is actively participating in the SEI formation where CF_3 and CF_2 are found at 293.2 eV and 291 eV, respectively. As a result, the more electronegative environment causes a significant shift in CO peak (286.9eV) and OCO (289.1 eV), which is demonstrated by the dashed line. This is further validated by the fluorine 1s spectra in Figure S5b and the higher binding energy peak shift of the S-O salt decomposition peaks, which are present between approximately 532 eV to 533 eV. There is a slight LiF peak shift to higher binding energy when comparing Gen II (684.8 eV) and SSEE (684.9 eV) to BSEE (685.3 eV).

Figure S8 shows the N 1s spectra for SSEE and BSEE SEI generated after the first deposition. The BSEE SEI contains large quantities of F-NSO_2 functionalities at compared to the SSEE SEI. The decomposition of LiFSI promotes the formation of N-S fragments and more NSO_2 compared to the BSEE SEI. Based on the counts, the BSEE SEI contains more salt decomposition products which can be attributed to the high salt concentration. This is consistent with the S 2p spectra, shown in Figure 5(e-h). Our previous work shows decomposition products associated with LiFSI reduction.[1] This is further demonstrated in this work as well as in the literature.[2, 7] However, the peaks located at 161 eV and 159 eV are not present in the SEI of the BSEE SEI. This is largely attributed to the LiTFSI contribution in the concentrated electrolyte.

Table S4. XPS Atomic Composition of region scans of O1s and S2p obtained from Figure 5.

Atomic Percentage	Oxygen 1s			Sulfur 2p				
Electrolyte: First deposition	**S-O**	**C-O**	**Li_2O**	**SO_3**	**NSO_2**	**FSO_2**	**Li_2SO_3**	**Li_2S/ S-S (LiFSI Reduction)**
SSEE	29.13	68.60	2.27	42.17	25.07	21.41	10.52	0.82
BSEE	89.48	10.52	0	47.34	28.33	20.46	3.87	0
Electrolyte: 200 cycles								
SSEE	54.25	22.42	23.33	34.56	24.42	0	0	41.02
BSEE	76.12	15.13	8.75	53.48	25.89	0	0	20.64

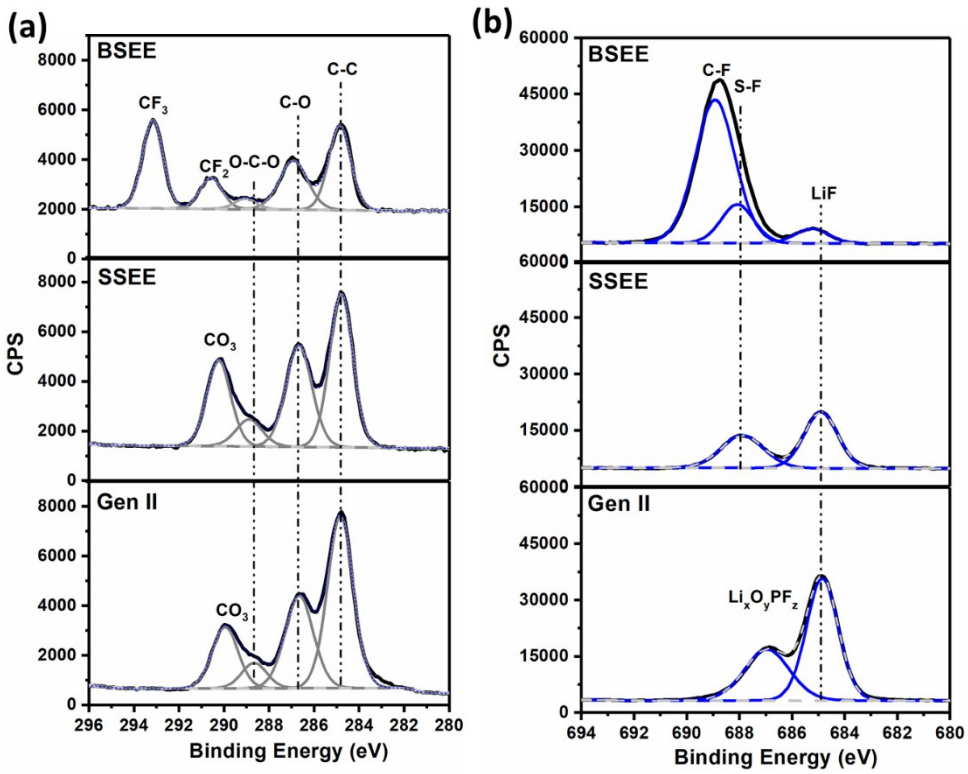

Figure S5. Region scans of C1s (a) and F1s (b) on plated lithium metal after the first cycle for BSEE, SSEE, and Gen II.

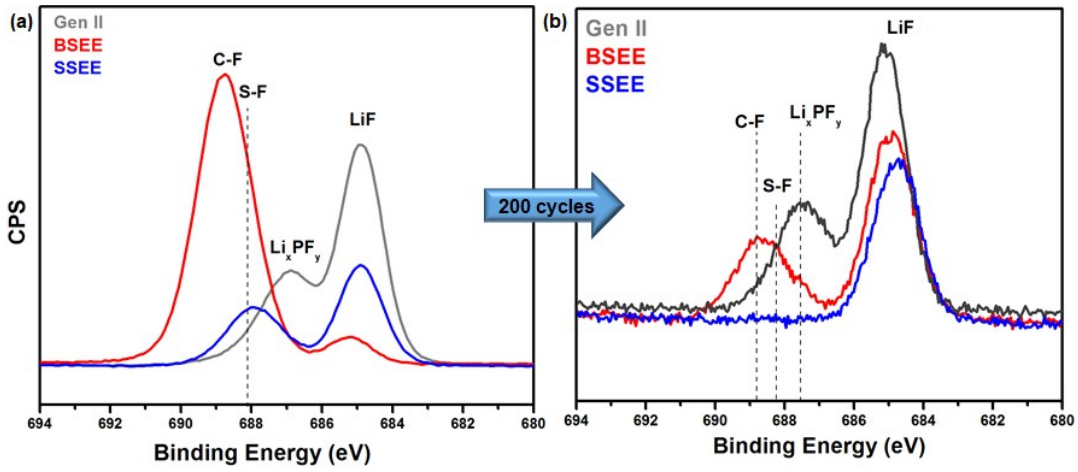

Figure S6. Region scans of Fluorine 1s (a) on plated lithium metal after the first deposition and (b) at the 200th deposition.

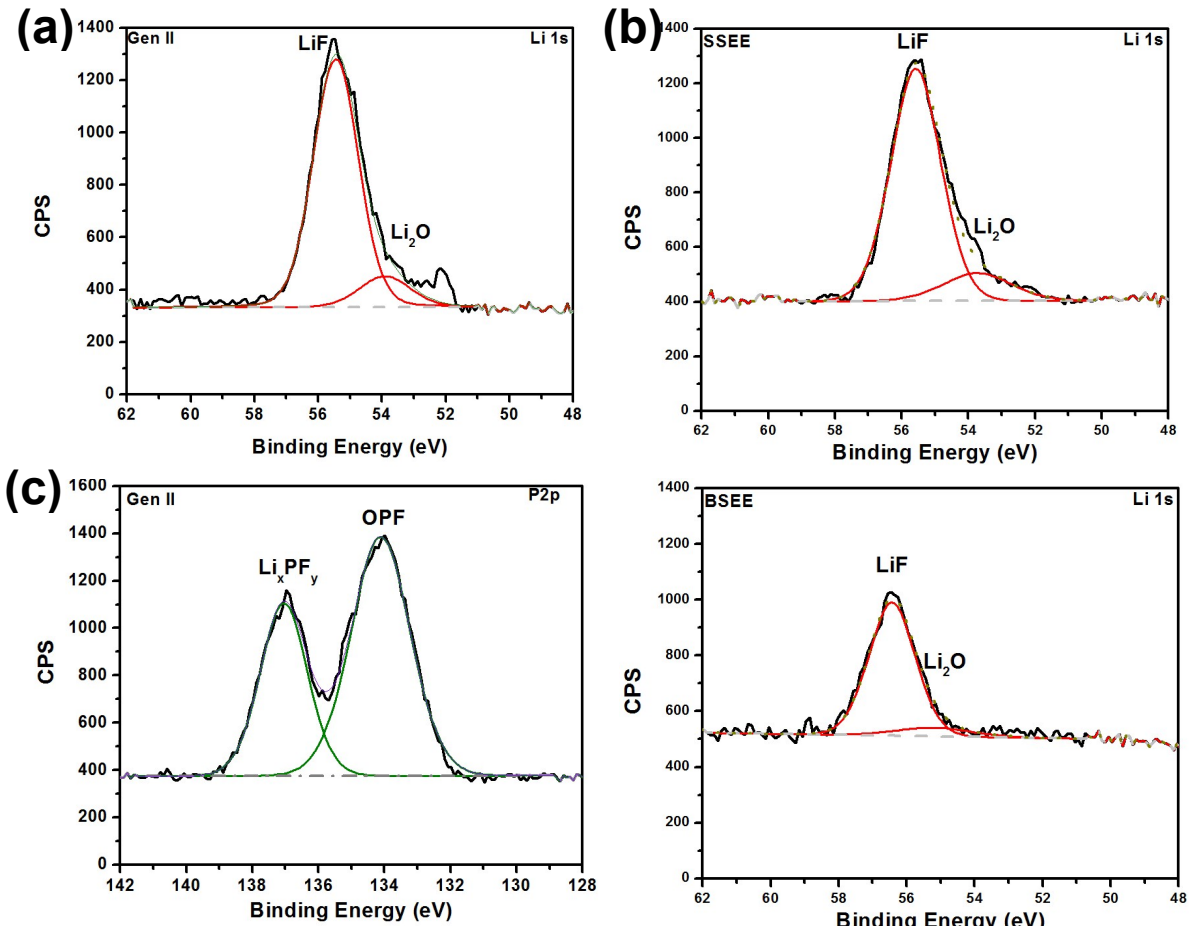

Figure S7. Region scans of lithium 1s (a,b,d) and phosphorus 2p (c, Gen II only) on plated lithium metal after the first deposition.

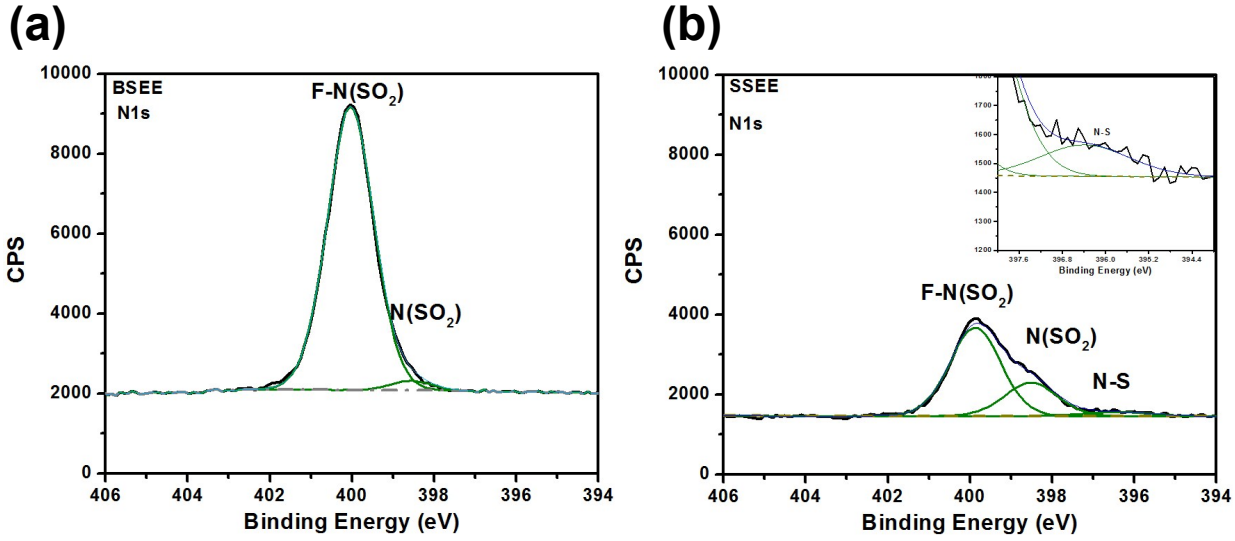

Figure S8. Region scans of nitrogen 1s on plated lithium metal after the first deposition.

Anodic Stability of Ether-based Electrolytes

Oxidative stability of the ether-based electrolytes doped with LiFSI and LiTFSI salts and molten salts was recently examined. LSV of 4M LiFSI-DME on Pt showed an onset of the initial oxidation current around 4.5 V, [2] while 7M LiTFSI-DME encapsulated in an organic framework exhibited currents below 1 μA cm^{-2} at 4.5 V and less than 10 μA cm^{-2} at 5 V on Pt vs. Li/Li^+.[8] The Watanabe group also reported significant stability against oxidation (>5 V vs. Li/Li^+ (current below 50 μA cm^{-2} on Pt at 5 V vs. Li/Li^+))of highly concentrated equimolar mixtures of LiTFSI(triglyme). Low concentration $(triglyme)_{20}LiTFSI$ was stable to around 4.5 V with an oxidation onset current at 3.7 V vs. Li/Li^+[9] that is consistent with the previously reported oxidation stability of low concentration ether-based electrolytes below 4 V.[10] The intrinsic oxidative stability of the $TFSI^-$ anion in a molten salt(x_{LiTFSI} = 0.20, x_{KTFSI} =0.10, xCs_{TFSI} = 0.70) was reported around 5 V on Pt (10 mV/s) scan.[11] The hybrid anion between TFSI and FSI Li[fTfN] Li(fluorosulfonyl)-(trifluoromethylsulfonyl)amide anion ($[(FSO_2)(CF_3SO_2)N]^-$, $fTfN^-$) has a similar oxidative stability in the motel salt regime as $TFSI^-$, which is consistent with similar oxidative stability of the $TFSI^-$ and FSI^- anions obtained in QC calculations.[12]

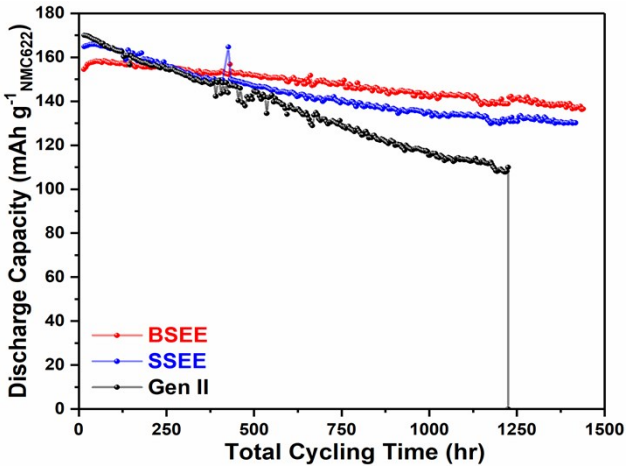

Figure S9. Replot of Figure 7b vs. total cycling time. BSEE/SSEE were stopped at 300 cycles, and the Gen II cell failed on the 274th cycle. The NMC electrodes had a mass loading of 1.44mAh cm^{-2}.

Table S5. Coulombic efficiency values for the Anode-free (NMC-622 vs Cu) cells after the first cycle, the last (54th) cycle, and the total average for each electrolyte composition.

Average Coulombic Efficiencies (NMC 622 vs. Cu)		
Cycles Sampled	**SSEE**	**BSEE**
1st Cycle	78.14%	80.51%
Last Cycle (54)	97.36%	98.63%
All 54 cycles	97.19%	98.37%

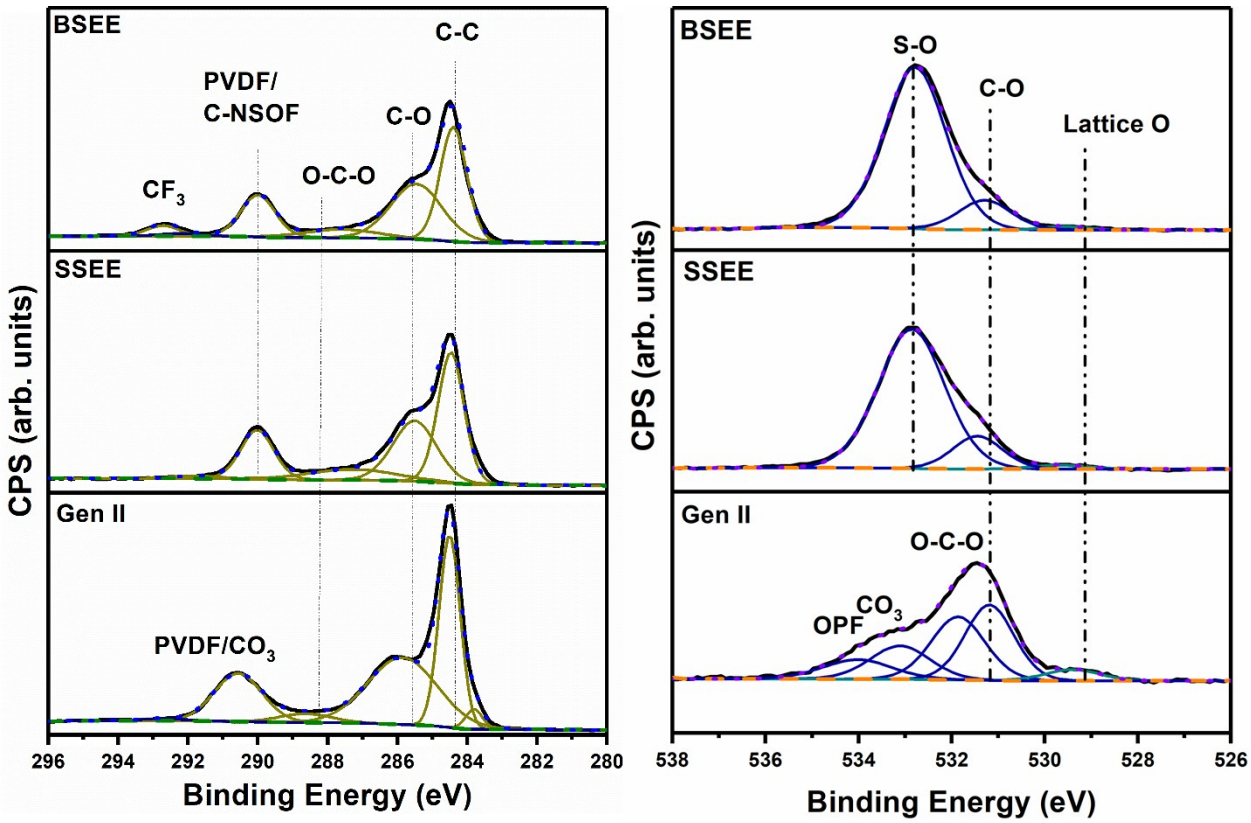

Figure S10. C1s (left) and O1s (right) of NMC622 CEI after 200 cycles in BSEE (top), SSEE (middle), and Gen II (bottom).

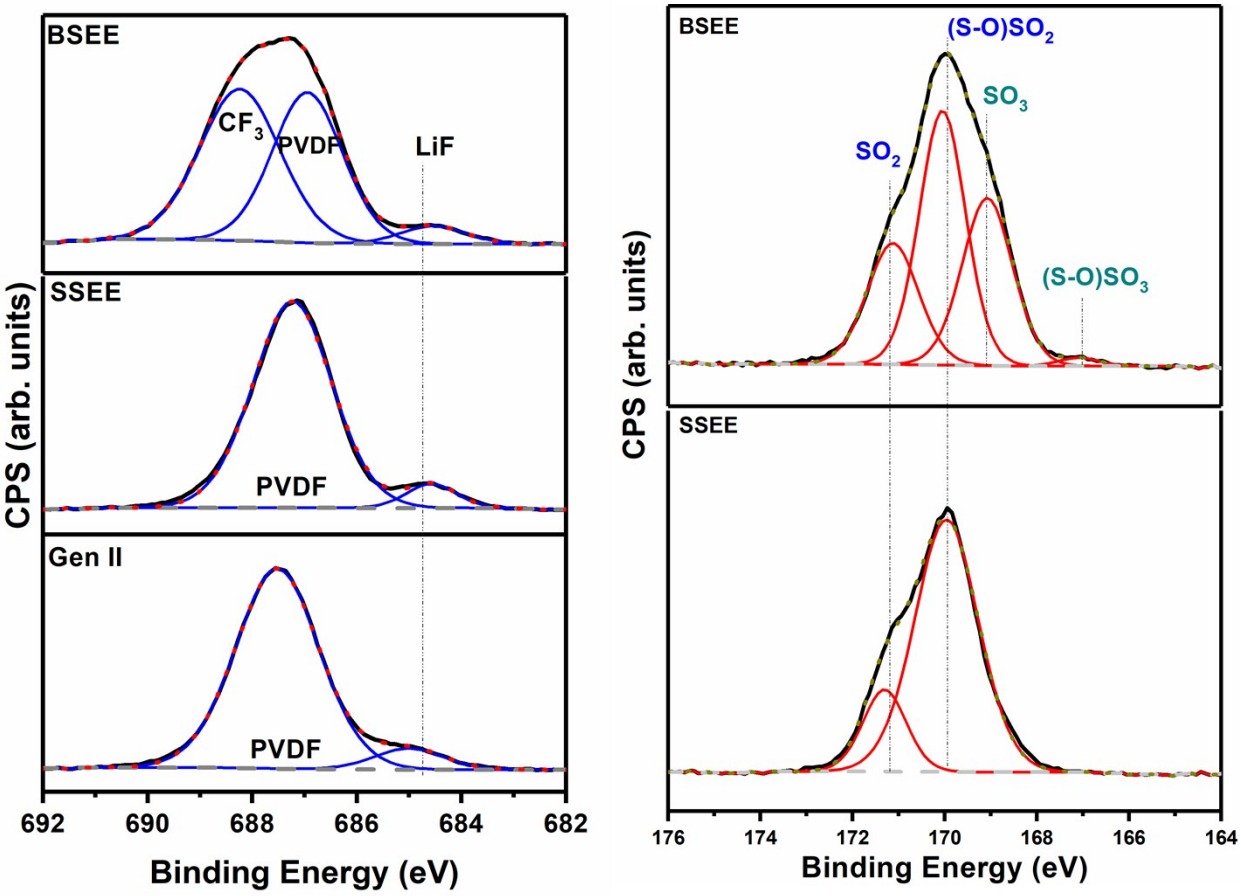

Figure S11. F1s (left) and S2p (right) of NMC622 CEI after 200 cycles.

Reduction of BSEE on Li|LiF

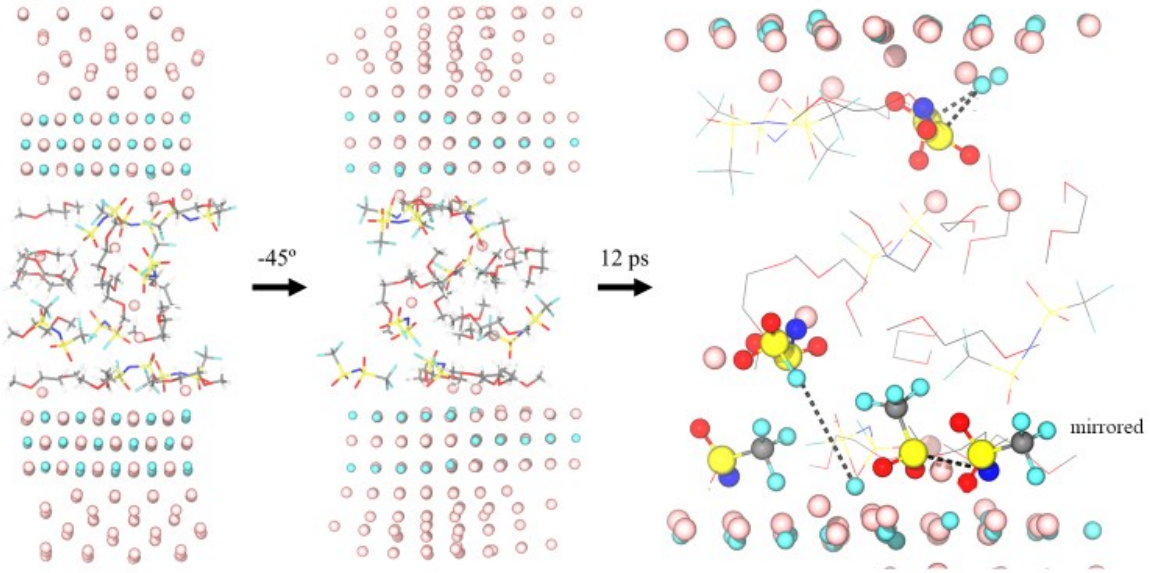

Figure S12. Large snapshot taken from one of the BOMD trajectories showing the reactions that took place on the Li|LiF interface. Some parts clipped by the periodic boundary are mirrored to complete any clipped anions. The initial configuration is shown on the far left. A -45° rotation was done to assist in visualization of the final snapshot. See caption of Figure 6 in main text for additional details.

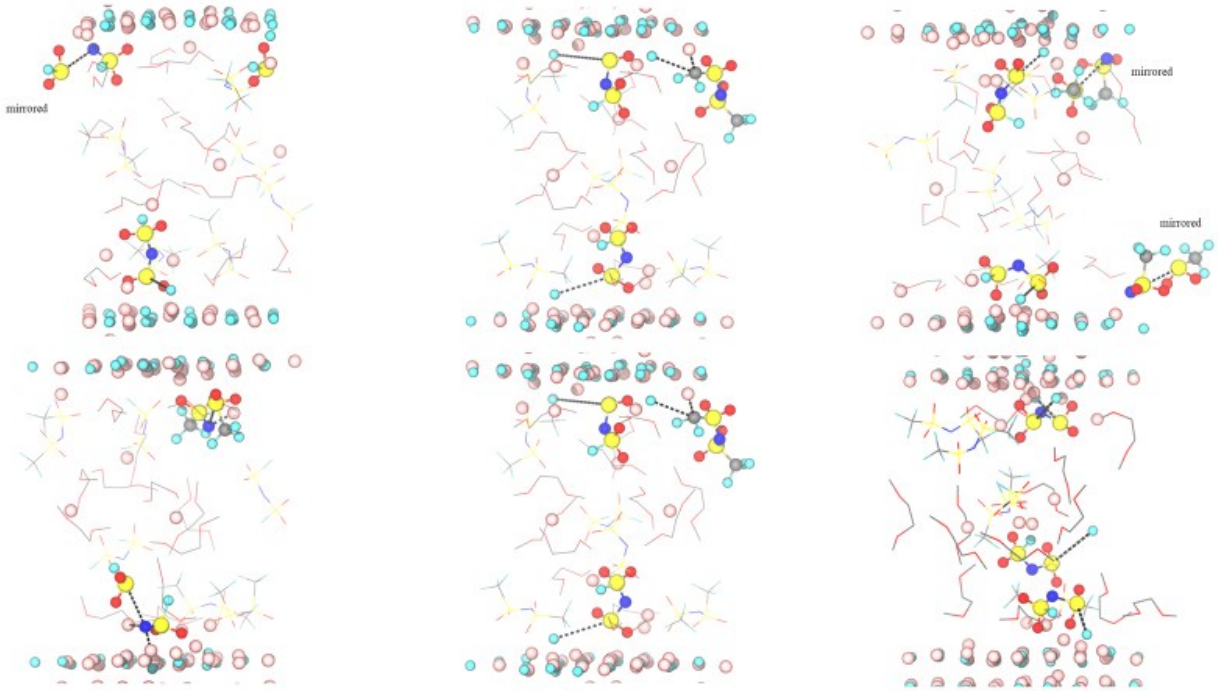

Figure S13. Final snapshots from each of the remaining 6 trajectories. See caption of Figure 6 in main text for additional details.

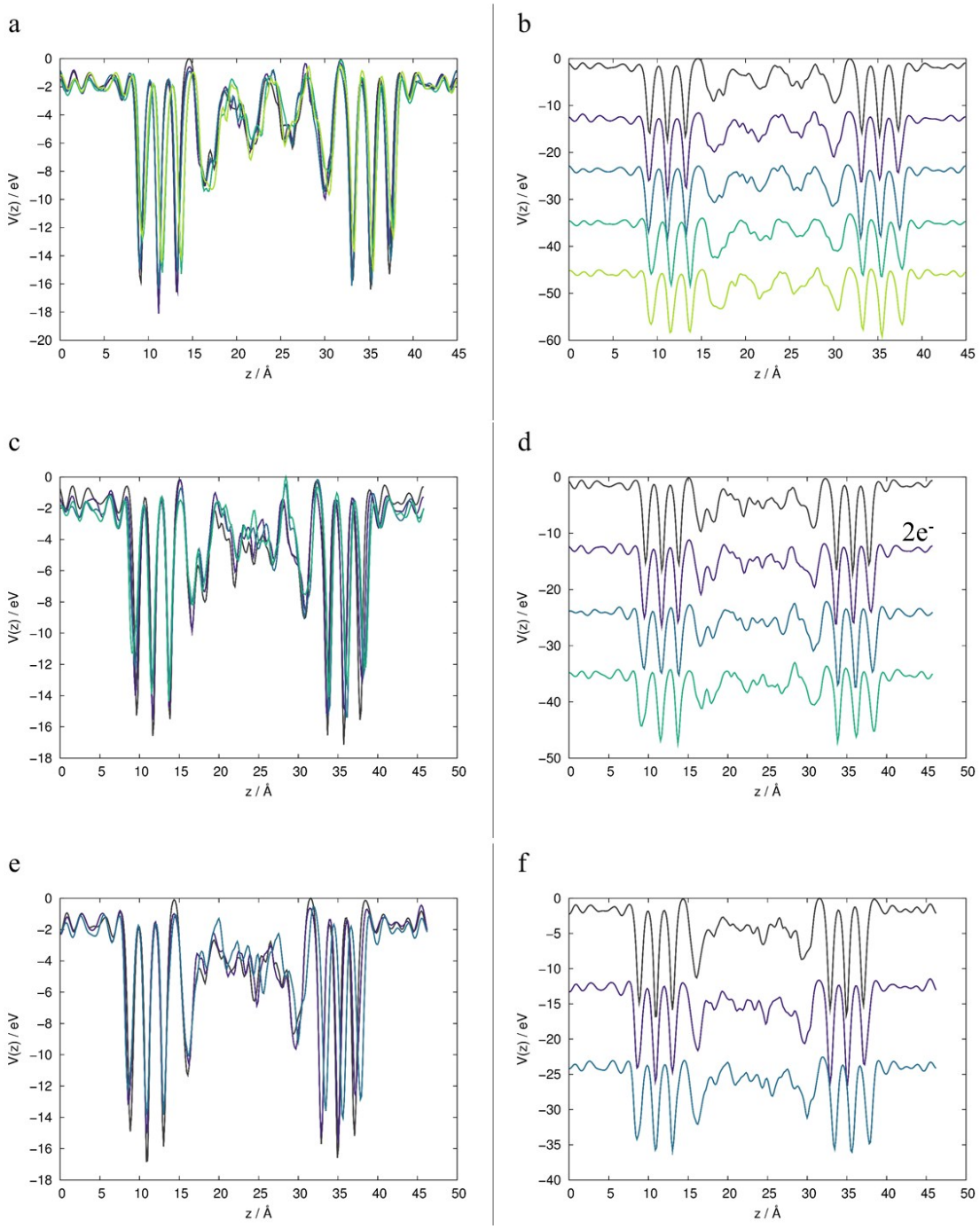

Figure S14. (a, c, e) Superposition of time- and plane-averaged electrostatic potentials through the cell, perpendicular to the Li|LiF interface for runs 2, 3, and 4; refer to Table 1 in main text. (b, d, f) Shifted electrostatic potentials for clarity. Color and shift reflect the number of electrons having been transferred to the electrolyte, from 0 to n. The influence of the electric double layer at the LiF|electrolyte interface on the electrostatic potential is shown in the circled regions.

Oxidation of DME solvent on Li_xNiO_2

Figures from DFT calculations showing for $Li_{0.5}NiO_2$ the transfer of H to a surface O and chemisorption of the DME fragment through a C-O bond. The radical could not be isolated without introducing unphysical constraints. Chemisorption is shown for two termination states. The O-H can either be projected into vacuum/electrolyte or be partially incorporated into the lattice. Under the latter conditions, Li migrates to an interstitial site. Only the first of these two states was observed for $LiNiO_2$. Reaction energies are relative to the adsorbed, unreacted state so always the first structure has a $\Delta E = 0$ eV.

The O-H bonds are shown twice across the periodic boundary of the crystal to more clearly visualize the Li migration. Only a single O-H bond is present in the calculations.

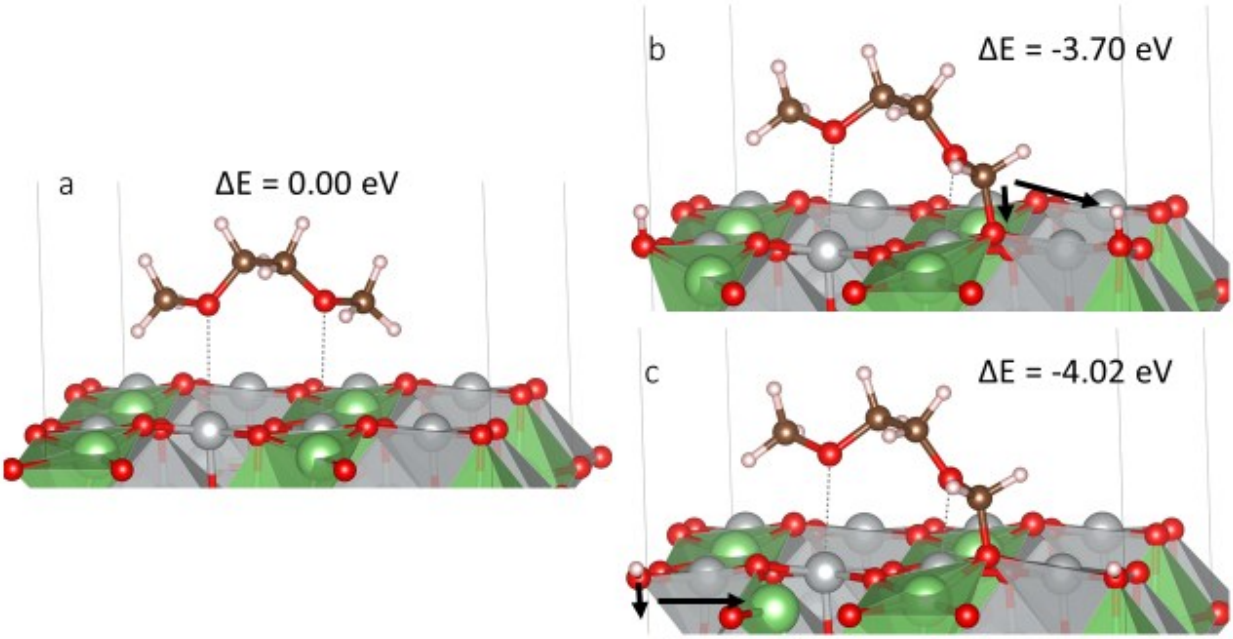

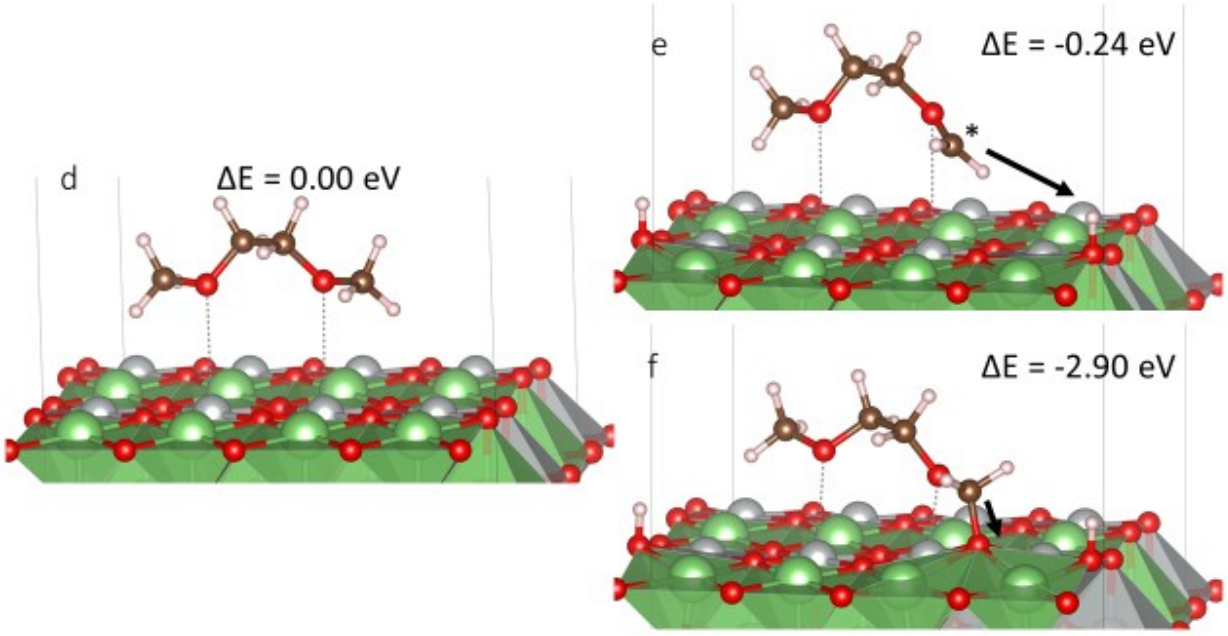

Figure S15. (a-c) DME decomposition on $Li_{0.5}NiO_2$. (d-f) DME decomposition on $LiNiO_2$.

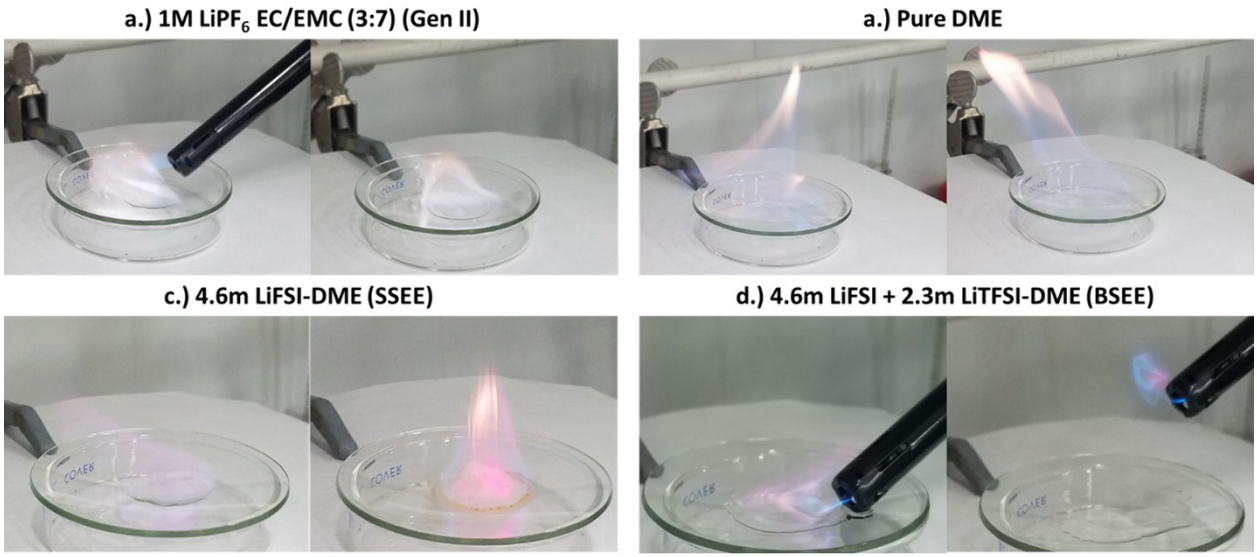

Figure S16. Rudimentary electrolyte safety analysis via flame test. ~10 drops (~1mL) of each electrolyte were dropped onto a watchglass and exposed to a butane candle lighter flame. The image on the left is immediately after flame exposure and the image on the right is a few seconds after the initial ignition. As expected, the Gen II (a) and pure DME solvent (b) were highly flammable and continued to burn aggressively after removal of the flame. The SSEE (c) initially produced a blue flame that evolved into a bright red flame before extinguishing and leaving a brown residue on the watchglass. The BSEE (d) produced a small blue flame briefly during the initial ignition that self-extinguished after the torch was removed. These results, though rudimentary, suggest that the addition of LiTFSI may provide a promising direction toward improving the safety of concentrated LiFSI and/or ether electrolytes like SSEE; however, we can make no claims regarding the safety of this approach in actual cells, particularly if they are high capacity.

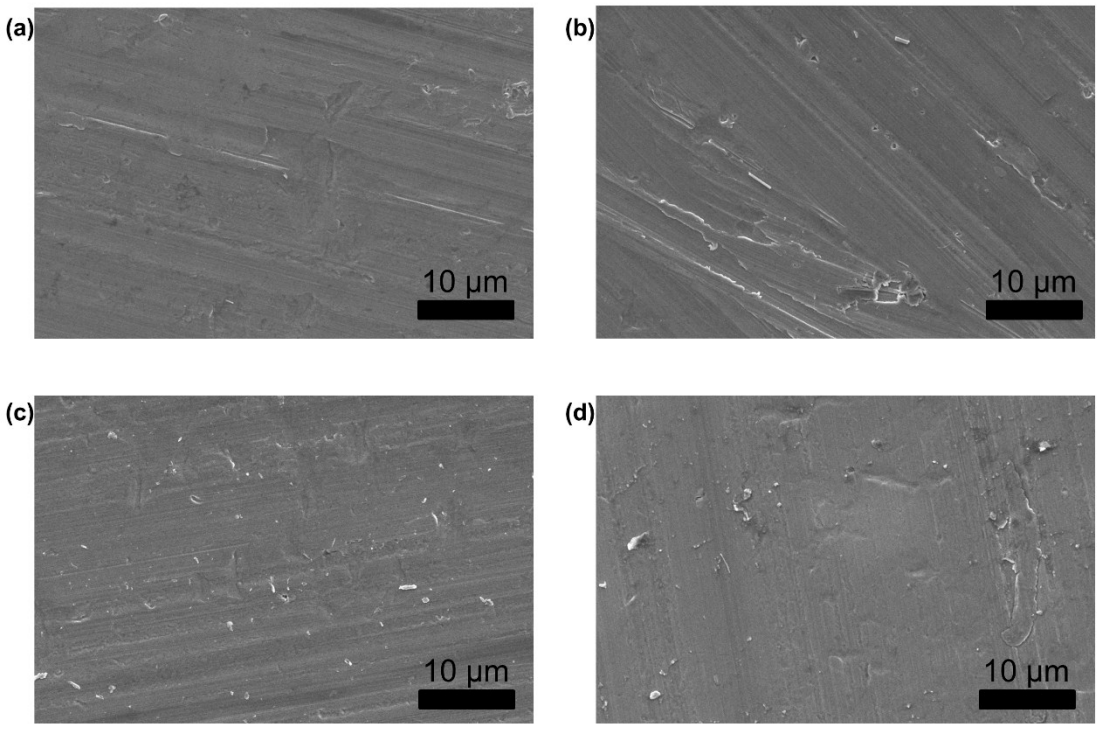

Figure S17: SEM images of NMC622 Al current collector backside (a) in the pristine state (b) after 50 cycles in SSEE (c) after 50 cycles in BSEE, and (d) after 200 cycles in BSEE. These images suggest minimal Al corrosion under these conditions, though the possibility of corrosion occurring after long term cycling or on the active material side of the current collector[1] warrants future investigation.

References:

1. J. Alvarado, M. A. Schroeder, M. H. Zhang, O. Borodin, E. Gobrogge, M. Olguin, M. S. Ding, M. Gobet, S. Greenbaum, Y. S. Meng and K. Xu, *Mater Today*, 2018, **21**, 341-353.
2. J. Qian, W. A. Henderson, W. Xu, P. Bhattacharya, M. Engelhard, O. Borodin and J. G. Zhang, *Nat Commun*, 2015, **6**, 6362.
3. O. Borodin, G. A. Giffin, A. Moretti, J. B. Haskins, J. W. Lawson, W. A. Henderson and S. Passerini, *J Phys Chem C*, 2018, **122**, 20108-20121.
4. O. Borodin, L. Suo, M. Gobet, X. Ren, F. Wang, A. Faraone, J. Peng, M. Olguin, M. Schroeder, M. S. Ding, E. Gobrogge, A. von Wald Cresce, S. Munoz, J. A. Dura, S. Greenbaum, C. Wang and K. Xu, *ACS Nano*, 2017, **11**, 10462-10471.
5. O. Borodin, *J Phys Chem B*, 2009, **113**, 11463-11478.
6. O. Borodin and G. D. Smith, *J Phys Chem B*, 2009, **113**, 1763-1776.
7. H. Kim, F. X. Wu, J. T. Lee, N. Nitta, H. T. Lin, M. Oschatz, W. I. Cho, S. Kaskel, O. Borodin and G. Yushin, *Advanced Energy Materials*, 2015, **5**, 1401792.
8. A. Petronico, T. P. Moneypenny, 2nd, B. G. Nicolau, J. S. Moore, R. G. Nuzzo and A. A. Gewirth, *J Am Chem Soc*, 2018, **140**, 7504-7509.
9. K. Yoshida, M. Nakamura, Y. Kazue, N. Tachikawa, S. Tsuzuki, S. Seki, K. Dokko and M. Watanabe, *J Am Chem Soc*, 2011, **133**, 13121-13129.
10. V. Etacheri, R. Marom, R. Elazari, G. Salitra and D. Aurbach, *Energy & Environmental Science*, 2011, **4**, 3243-3262.
11. A. Watarai, K. Kubota, M. Yamagata, T. Goto, T. Nohira, R. Hagiwara, K. Ui and N. Kumagai, *J Power Sources*, 2008, **183**, 724-729.
12. O. Borodin, W. Behl and T. R. Jow, *J Phys Chem C*, 2013, **117**, 8661-8682.